Attribution of direct ozone radiative forcing to spatially resolved emissions

K. Bowman[1] and D. K. Henze[2]

Received 25 July 2012; revised 9 October 2012; accepted 18 October 2012; published 29 November 2012.

[1] Quantifying the dependence of ozone direct radiative forcing (DRF) on the mixture and spatial distribution of precursor emissions is a key step towards understanding the impact of air quality standards on climate. We use here a combination of satellite observations of ozone and its radiative effect in conjunction with an adjoint chemical transport model to determine the ozone DRF due to global, anthropogenic NO_x, CO, and non-methane hydrocarbons (NMHC) emissions regionally at $2^\circ \times 2.5^\circ$ regions resolution. We show that 8% of the ozone DRF from the sum of all these emissions can be attributed to 15 regions, which are predominantly located in China and the United States (US). To achieve an equivalent reduction in ozone DRF, necessary emission reductions for each precursor vary intra-continentally by a factor of 3–10 and globally by over an order of magnitude. The contribution of NO_x emissions to ozone DRF relative to CO and NMHC emissions within individual regions varies globally by nearly a factor of two. **Citation:** Bowman, K., and D. K. Henze (2012), Attribution of direct ozone radiative forcing to spatially resolved emissions, *Geophys. Res. Lett.*, *39*, L22704, doi:10.1029/2012GL053274.

1. Introduction

[2] Air quality and climate co-benefit strategies for ozone are complicated by the complex spatio-temporal structure of tropospheric ozone and the non-linear chemistry relating precursor emissions to ozone distributions [*Forster et al.*, 2007; *Levy et al.*, 2008; *Sitch et al.*, 2007; *Kawase et al.*, 2011]. Previous studies have focused on climate responses to continental-scale radiative forcing (RF) [*Shindell and Faluvegi*, 2009], the role of sectorally aggregated [*Unger et al.*, 2010; *Fuglestvedt et al.*, 2008] and continental-scale [*Naik et al.*, 2005; *Berntsen et al.*, 2006; *Stevenson and Derwent*, 2009] changes in precursor emissions on RF, and the degree to which increases in CH_4 radiative forcing following NO_x reductions can offset reduced ozone direct radiative forcing [*Naik et al.*, 2005; *Fiore et al.*, 2008; *Derwent et al.*, 2008; *Stevenson and Derwent*, 2009].

[3] In this work we address the role of regional ($2^\circ \times 2.5^\circ$) variations in chemical environment and transport in modulating direct ozone radiative forcing (DRF) at intra-continental scales through a novel approach that uses satellite observations from the Tropospheric Emission Spectrometer (TES) in conjunction with adjoint sensitivity analysis from the GEOS-Chem chemistry and transport model. Observationally constrained radiative forcings are calculated in each grid-cell for more than thirty different emission types, including both natural and sector-specific anthropogenic O_3 precursors; we focus here on anthropogenic NO_x, CO, and NMHC sources because of their dominant role in ozone photochemistry and air quality (contributions of sector-aggregated NO_x emissions are provided in Table S1 in Text S1 in the auxiliary material).[1] This level of quantification is made feasible through the use of an adjoint model, which in general is an efficient means of calculating sensitivities with respect to large numbers of model inputs (in this case emissions). This approach, however, only accounts for ozone direct RF, which does not include methane-ozone feedbacks or indirect methane RF. These additional effects have a significant impact on total RF from precursor emissions and would need to be included in any comprehensive air quality-climate co-benefit analysis.

2. Methods

2.1. Tropospheric O_3 Radiative Effects Using TES IRKs

[4] The Tropospheric Emissions Spectrometer (TES) is a polar sun-synchronous, high resolution (0.1 cm^{-1} apodized), infrared Fourier transform spectrometer aboard the NASA Aura satellite with a global repeat cycle of 16 days and an averaged nadir footprint of 5 km × 8 km [*Beer*, 2006]. Vertical ozone profiles are derived from spectrally-resolved top-of-the-atmosphere (TOA) thermal radiances based on an optimal estimation framework [*Bowman et al.*, 2006]. This relationship between TOA radiances and ozone distributions was first exploited to quantify the greenhouse gas effect of upper tropospheric ozone over clear-sky, oceanic scenes [*Worden et al.*, 2008] but was subsequently formalized for all-sky and land/oceans scenes through the introduction of longwave instantaneous radiative kernels (IRK) defined as

$$\mathbf{k}_i = \frac{\partial F_i}{\partial \mathbf{c}_i} \tag{1}$$

where F_i is the instantaneous upward TOA flux in atmospheric column location i integrated across the infrared band in W/m^2, $\mathbf{c}_i$ is the TES retrieved ozone profile on L pressure levels, and $\mathbf{k}_i$ is the IRK in W/m^2/ppb of the ith column.

[1]Jet Propulsion Laboratory, California Institute of Technology, Pasadena, California, USA.
[2]Department of Mechanical Engineering, University of Colorado Boulder, Boulder, Colorado, USA.

Corresponding author: K. Bowman, Jet Propulsion Laboratory, California Institute of Technology, 4800 Oak Grove Dr., Pasadena, CA 91109, USA. (kevin.w.bowman@jpl.nasa.gov)

0094-8276/12/2012GL053274

[1]Auxiliary materials are available in the HTML. doi:10.1029/2012GL053274.

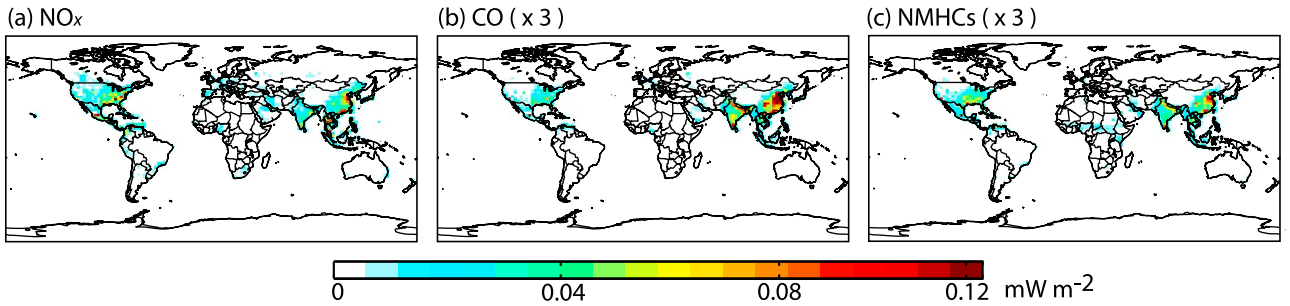

Figure 1. Ozone direct radiative forcing (DRF), $\boldsymbol{\lambda}$, as attributed from TES observations for August 2006 emissions to each grid cell of (a) NO_x (b) CO (scaled by 3) and (c) NMHC (scaled by 3). The color scale is saturated for DRF > 0.12 mW/m^2.

Under clear-sky scenes, the global mean IRK peak sensitivity for August 2006 is about 0.6 mW/m^2/ppb at around 550 hPa, decreasing linearly in pressure towards the surface and the tropopause. TES ozone and IRKs have been applied to chemistry climate model evaluation [*Aghedo et al.*, 2011a] and TES sampling has been shown to be sufficiently accurate to estimate zonal monthly mean distributions to within a few ppb [*Aghedo et al.*, 2011b]. The unweighted global mean of the all-sky longwave radiative effect, which includes both natural and anthropogenic ozone, is 0.33 ± 0.02 W/m^2 [*Worden et al.*, 2011] . The longwave radiative effect from TES is less than most estimates of the anthropogenic component (i.e., radiative forcing) alone [*Forster et al.*, 2007]. These differences can be attributed in part to definitions of radiative forcing, which is commonly defined at the tropopause, spans the shortwave (SW) and long wave (LW) spectrums, and includes stratospheric temperature adjustment. The SW is generally a small contribution to ozone RF. The instantaneous TOA RF is about 10–20% higher than the stratospherically adjusted RF depending on the model [*Forster et al.*, 2007].

2.2. GEOS-Chem Forward and Adjoint Model

[5] GEOS-Chem (*www.geos-chem.org*) is a chemical transport model primarily driven by assimilated meteorology from the Goddard Earth Observing System (GEOS) of the NASA Global Modeling and Assimilation Office (GMAO). The spatial resolution of the GEOS meteorological fields are reduced to facilitate detailed simulation of tropospheric gas-phase HO_x-NO_x-VOC chemistry [*Bey et al.*, 2001]. For this work, we use model v8-02-01 with relevant updates through v9-01-01, run at the global 2° × 2.5° resolution. Global anthropogenic emissions of NO_x are from EDGAR [*Olivier et al.*, 2001], overwritten by regional inventories in specific areas [*van Donkelaar et al.*, 2008]. Monthly biomass burning emissions are from GFEDv2 [*van der Werf et al.*, 2009] and biofuel emissions from *Yevich and Logan* [2003]. The adjoint of GEOS-Chem [*Henze et al.*, 2007] solves a set of equations auxiliary to the forward chemical transport model in a manner that efficiently yields the gradient of a scalar forward model response function with respect to all model parameters simultaneously. The adjoint has been used for analyzing long-rang impacts on O_3 [*Zhang et al.*, 2009; *Walker et al.*, 2012] as well as O_3 assimilation [*Singh et al.*, 2011; *Parrington et al.*, 2012].

2.3. Ozone Radiative Forcing

[6] We first define the mean area weighted observed outgoing TOA longwave radiative forcing:

$$\mathcal{J} = \frac{1}{A}\sum_{i}^{N} a_i F_i \tag{2}$$

where F_i is the ith of N TOA fluxes measured by the TES satellite. The product is weighted by the area of the model grid, a_i, and normalized by the total area, $A = \sum_i^N a_i$. The sensitivity of the mean TOA flux to emissions of each ozone precursor in each model grid cell is then

$$\boldsymbol{\lambda} = \nabla_{\mathbf{E}}\mathcal{J} \tag{3}$$

where $\mathbf{E}$ is a vector of emissions from each species, sector and in each grid cell. Equation (3) is the direct ozone radiative forcing when E is anthropogenic. λ_i, The sensitivity in equation (3) can be calculated for any single observed TOA flux from TES, F_i (extension to the global mean TOA flux, $\mathcal{J}$, is straightforward) as

$$\boldsymbol{\lambda}_i = \frac{a_i}{A}\frac{\partial F_i}{\partial \mathbf{E}} = \frac{a_i}{A}\left(\frac{\partial \mathbf{c}_i}{\partial \mathbf{E}}\right)^T \frac{\partial F_i}{\partial \mathbf{c}_i}, \tag{4}$$

where the chain rule is employed to separate the sensitivity of flux to concentrations and the sensitivity of concentrations to emissions. The product of the two terms on the far right hand of equation (4) is calculated by the adjoint model [see *Henze et al.*, 2007]. The novelty of our approach is to use the observationally derived TES IRK's (equation (1)) to quantify the derivative of the observed flux with respect to retrieved ozone profiles, and to then propagate this sensitivity efficiently backwards in time using an adjoint model to obtain sensitivities with respect to emissions. The adjoint sensitivities of the August DRF are integrated backwards through the beginning of July, by which time they asymptotically approach steady state values owing to the lifetime of tropospheric O_3. As shown in Figure S1, adjoint estimates for ozone DRF from the emissions in individual grid cells are in consistent agreement with evaluation of the full forward model across a wide range of emission perturbations with a slope of 0.991 and R^2 = 0.993, and the adjoint-based forcings are additive for modest changes to emissions across broader scales.

3. Results

[7] The sensitivities of the outgoing longwave radiation at the top-of-the-atmosphere (TOA) as observed by TES with respect to spatially-resolved anthropogenic NO_x, CO, and

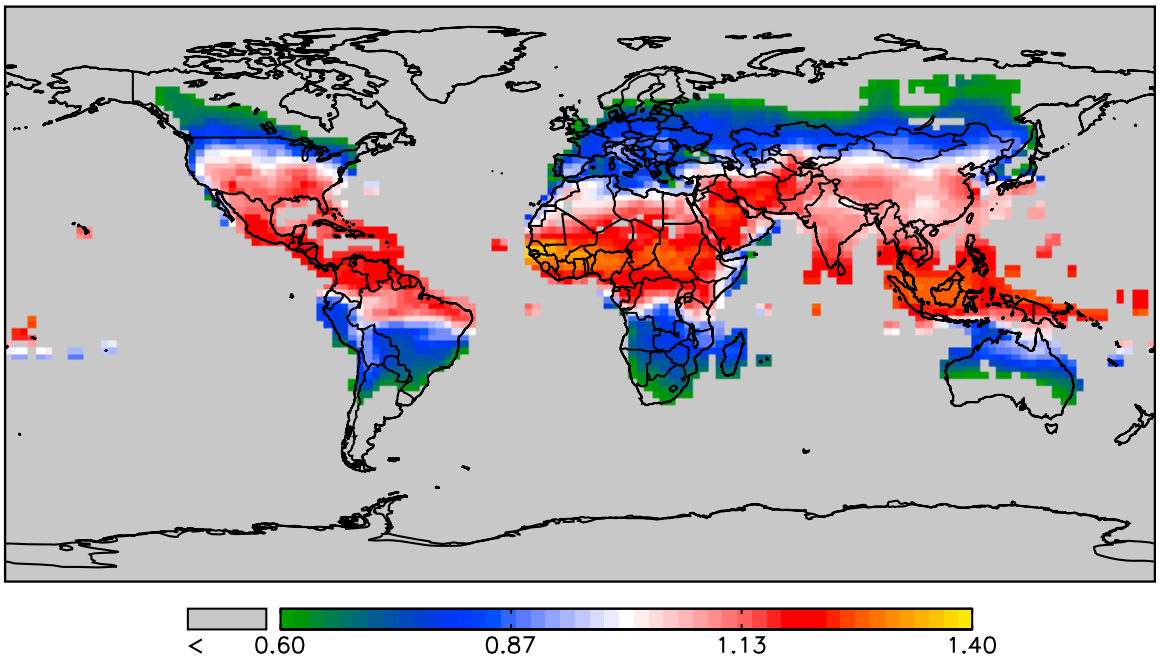

Figure 2. The impact of NO_x emission locations on ozone DRF. Areas where the radiative effectiveness ratio, r_{eff}, is greater (less) than one indicate regions where additional NO_x emissions would lead to an amplified (diminished) mean global ozone radiative forcing relative to the change in mean global ozone.

NMHC emissions are shown in Figure 1. These global emissions are defined on a 2° × 2.5° grid, which we refer to as "regions." We note that this observationally derived radiative forcing at the TOA is significantly lower [*Worden et al.*, 2008] than typical values modeled at the tropopause [*Forster et al.*, 2007]. We have focused on August, 2006, which is the seasonal maximum in ozone radiative forcing for North America and consequently represents the strongest diversity of forcing responses to emissions [*Naik et al.*, 2005]. There are 15 2° × 2.5° regions with a combined radiative forcing greater than 0.15 mW/m^2, which represents about 8% of ozone DRF from all anthropogenic emissions. For brevity, we denote these 2° × 2.5° regions by the names of the major city contained therein. Regions within China accounts for 10 of these and includes the Shanghai region, which is globally the most important: 0.31 (0.20 (NO_x), 0.07 (CO), 0.04 (NMHC)) mW/m^2. While NO_x emissions are usually the dominant radiative forcing in any single location, the Henan provence centered near Zhoukou (34°N, 115°E) is distinguished by a larger impact of CO and NMHC (56%) versus NO_x emissions (44%) to its total radiative forcing of 0.16 mW/m^2. The US contribution includes Houston 0.17 (0.12 (NO_x), 0.02 (CO), 0.03 (NMHC)), New Orleans 0.16 (0.12 (NO_x), 0.02 (CO), 0.02 (NMHC)), and Western Atlanta 0.16 (0.11 (NO_x), 0.02 (CO), 0.02 (NMHC)). The remaining regions are Mexico City 0.27 (0.16 (NO_x), 0.04 (CO), 0.07 (NMHC)) and Kuala Lumpur 0.15 (0.13 (NO_x), 0.01 (CO), 0.01 (NMHC)). The impact of these latter regions is accentuated by their efficient transport pathways to the upper troposphere. Consistent with previous studies [*Naik et al.*, 2005], high latitude regions, such as in Europe, play a minor role in direct ozone radiative forcing despite having comparable emission levels.

[8] The heterogeneity in ozone DRF for August 2006 as shown in Figure 1 is a function of several factors: the season, the magnitude of the underlying emissions in each grid-cell, the photochemical efficiency of O_3 formation in a given location per amount of precursor emitted, the transport of ozone into the free troposphere and the underlying distribution of clouds, water vapour, and temperature. In order to isolate the role of the physical atmospheric structure relative to the emission magnitude, we define a radiative forcing efficiency ($r_{eff}(x, y)$) as a ratio of the global mean ozone DRF sensitivity for a single emission location to the global mean ozone sensitivity to that same emission location. If, for example, changing NO_x emissions for a location by 100% leads to a 0.1% change in global mean ozone and a 0.125% change in global mean ozone DRF, then $r_{eff} = 1.25$.

[9] A plot of this radiative forcing efficiency is shown in Figure 2 for NO_x emissions. Differences are particularly striking between North America and Europe, with NO_x emissions from the former producing O_3 that is nearly twice as radiatively efficient. The meridional effect in radiative forcing efficiency [*Naik et al.*, 2005] leads to a maximum in the tropics, decreasing poleward by over a factor of two. In general, this ratio is highest in areas with convective lofting (i.e., the tropics) and over regions of higher altitude. However, there are important zonal variations that are related to cloud cover and convection. For example, r_{eff} is high (>1.2) over Saudi Arabia and Iran for August 2006 because surface temperatures are both very high and the regions are relatively cloud free. Changes in atmospheric circulation due to monsoons have a significant impact on the export of surface emissions to the free troposphere. The highest values of r_{eff} are due to the Western African Monsoon, which is related to the shift of the inter-tropical convergence zone northward from the tropical Atlantic ocean towards the Saharan desert. The strong poleward temperature gradient results in a complex circulation pattern leading to significant convection and export along both mid-level African and high-level Tropical

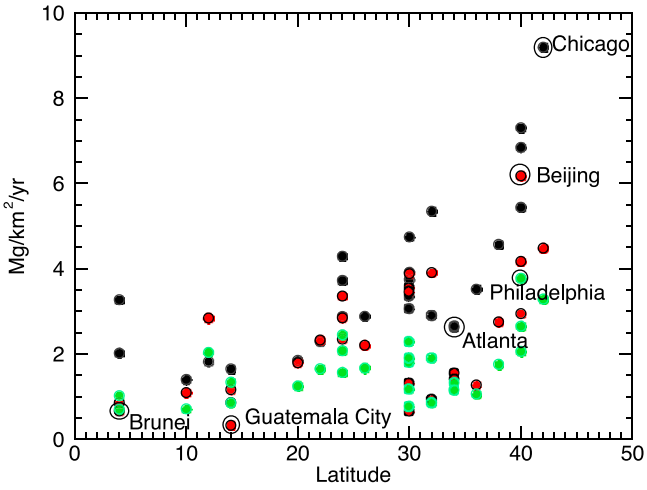

Figure 3. NO_x (black), CO (red), and NMHC (green) emissions that have about 0.1 ± 0.01 mW/m^2 DRF. CO emissions have been reduced by 10 to fit on the same scale. Selected cities represent 2° × 2.5° metropolitan regions and are identified adjacent to their respective emissions.

Easterly Jets [*Sauvage et al.*, 2007]. The onset of the Indo-Australian Monsoon is influenced by El Niño conditions and a complex air-land interaction [*Moron et al.*, 2009], but the region is convectively unstable for all seasons leading to a very high r_{eff}. Radiative forcing efficiencies of CO and NMHCs, which are available in Figure S2, have the same meridional gradient but a much more diffuse zonal distribution.

[10] The variability of r_{eff} on spatial resolutions at which air quality strategies are enacted in practice has important policy implications. To illustrate the potential of this approach for supporting policy analysis, 2° × 2.5° regions with approximately the same total DRF, i.e., the DRF from the sum of NO_x, CO, and NMHC emissions, of 0.1 ± 0.01 mW/m^2 are shown in Figure 3 (details shown in Table S2 in Text S1).

[11] Across the 27 regions matching this criteria, NO_x emissions represent about 64 ± 14% of the DRF. Emissions increase with latitude by roughly a factor of 5–20 depending on the precursor emissions with considerable zonal scatter. For example, the Guatemala City region has 10 times smaller NO_x emissions than Chicago and almost 20 times lower CO emissions than Beijing but correspond to the same total DRF. Similarly, the Brunei region near Malaysia has 5 times lower NMHC emissions than the Philadelphia region. These variations are driven by the poleward temperature gradient as well as cloud cover and large scale processes such as the Asian monsoon. Continental scale processes lead to a considerable spread in emissions as well. The region east of Atlanta (not to be confused with the Western Atlanta region discussed previously) has the lowest NO_x emissions of the 11 selected regions and is 3.5 times lower than Chicago. The enhanced sensitivity in the Southeastern US is associated with summertime convection [*Li et al.*, 2005], as shown by r_{eff} in the Figure S3. Consequently, the variability of US emissions with 0.1 mW/m^2 DRF is about half of the mean: 4.3 ± 2.1(NO_x), 21 ± 12 (CO), and 1.7 ± 1.0 (NMHC) Mg/km^2/yr. The choice of metrics used in an air-quality climate co-benefit analysis could lead to very different results based on this variability. For example, a 10% reduction in NO_x emissions in Chicago would lead to 0.01 mW/m^2 change in DRF but the equivalent absolute reduction to emissions east of Atlanta would lead to a 0.035 mW/m^2 DRF reduction. Consequently, controlling against emissions for air quality versus DRF for climate can lead to very different strategies depending on location. It is important to identify various approaches to attaining the targeted O_3 DRF as reductions in NO_x emissions will increase methane lifetime–a more efficient greenhouse gas–whereas reductions in CO and NMHC will decrease methane lifetime [*West et al.*, 2006].

[12] The accuracy of grid-scale radiative forcings is limited by a knowledge of precursor emission distributions and their ozone response, tracer transport, and the distribution of clouds. Nevertheless, such results can be aggregated and compared to previous studies. While the magnitude of the infrared, top-of-the-atmosphere ozone DRF reported here is smaller from ozone DRF defined at the tropopause by a factor of six, the relative sensitivity of ozone DRF to fractional emission changes aggregated to continental scales closely follows that of a previous work [*Naik et al.*, 2005] using different model emissions, chemistry and transport (see Figure S4). The agreement in relative sensitivity suggests that the differences are due to satellite versus model calculation of the ozone radiative effect rather than linearity assumptions in the adjoint approach.

4. Conclusion

[13] Overall, we have shown here that there is substantial variability in the radiative forcing of O_3 precursor emissions at regional scales, and that the combined use of remote sensing observations and adjoint modeling provides a means of characterizing such variability. Further, there is considerable variability in the extent to which different precursors (NO_x vs CO vs hydrocarbons) contribute to ozone's radiative impacts, as well as variability in the contribution of different emissions sectors within these species, which are critical for the overall O_3 response to emissions changes when accounting for the full range of chemical and physical feedbacks. Incorporation of climate co-benefits into air quality mitigation strategies thus requires quantitative understanding of chemical and physical processes at scales ranging from sub-continental to global.

[14] Equally important as design of control strategies is a framework to observe and assess the efficacy of these strategies against the backdrop of natural variability. While we do not address this framework explicitly, the satellite observations and assimilation system used in this study would be essential elements. The proposed suite of geo-stationary composition satellites from the Atmospheric Composition Constellation (ACC) as part of the Committee on Earth Observing Satellites (CEOS) (http://www.ceos.org) in conjunction with surface measurements could potentially provide the necessary observing system to support the implementation of ozone climate mitigation strategies. The requirements for such as system will be a point of future research.

[15] **Acknowledgments.** This research was carried out in part at the Jet Propulsion Laboratory, California Institute of Technology, under contract from NASA. We would like thank Helen Worden (NCAR) and the TES team for the IRK products. We acknowledge sponsorship from NASA AQAST (NNX11AI54G), AURA (NNH07ZDA001N), New Investigator Program (NNX10AR06G) and HEC computing facilities.

[16] The Editor thanks two anonymous reviewers for assistance evaluating this paper.

References

Aghedo, A. M., K. W. Bowman, H. M. Worden, S. S. Kulawik, D. T. Shindell, J. F. Lamarque, G. Faluvegi, M. Parrington, D. B. A. Jones, and S. Rast (2011a), The vertical distribution of ozone instantaneous radiative forcing from satellite and chemistry climate models, *J. Geophys. Res.*, *116*, D01305, doi:10.1029/2010JD014243.

Aghedo, A. M., K. W. Bowman, D. T. Shindell, and G. Faluvegi (2011b), The impact of orbital sampling, monthly averaging and vertical resolution on climate chemistry model evaluation with satellite observations, *Atmos. Chem. Phys.*, *11*(13), 6493–6514, doi:10.5194/acp-11-6493-2011.

Beer, R. (2006), TES on the Aura mission: Scientific objectives, measurements, and analysis overview, *IEEE Trans. Geosci. Remote Sens.*, *44*(5), 1102–1105.

Berntsen, T., J. Fuglestvedt, G. Myhre, F. Stordal, and T. Berglen (2006), Abatement of greenhouse gases: Does location matter?, *Clim. Change*, *74*(4), 377–411, doi:10.1007/s10584-006-0433-4.

Bey, I., D. J. Jacob, R. M. Yantosca, J. A. Logan, B. D. Field, A. M. Fiore, Q. Li, H. Y. Liu, L. J. Mickley, and M. G. Schultz (2001), Global modeling of tropospheric chemistry with assimilated meteorology: Model description and evaluation, *J. Geophys. Res.*, *106*(D19), 23,073–23,095.

Bowman, K. W., et al. (2006), Tropospheric emission spectrometer: Retrieval method and error analysis, *IEEE Trans. Geosci. Remote Sens.*, *44*(5), 1297–1307, doi:10.1109/TGRS.2006.871234.

Derwent, R., D. Stevenson, R. Doherty, W. Collins, M. Sanderson, and C. Johnson (2008), Radiative forcing from surface NO_x emissions: Spatial and seasonal variations, *Clim. Change*, *88*(3), 385–401, doi:10.1007/s10584-007-9383-8.

Fiore, A. M., J. J. West, L. W. Horowitz, V. Naik, and M. D. Schwarzkopf (2008), Characterizing the tropospheric ozone response to methane emission controls and the benefits to climate and air quality, *J. Geophys. Res.*, *113*, D08307, doi:10.1029/2007JD009162.

Forster, P., et al. (2007), Changes in atmospheric constituents and in radiative forcing, in *Climate Change 2007: The Physical Science Basis. Contributions of Working Group I to the Fourth Assessment Report on the Intergovernmental Panel on Climate Change*, edited by S. Solomon et al., pp. 129–234, Cambridge Univ. Press, Cambridge, U. K.

Fuglestvedt, J., T. Berntsen, G. Myhre, K. Rypdal, and R. B. Skeie (2008), Climate forcing from the transport sectors, *Proc. Natl. Acad. Sci. U. S. A.*, *105*(2), 454–458, doi:10.1073/pnas.0702958104.

Levy, H., II, M. D. Schwarzkopf, L. Horowitz, V. Ramaswamy, and K. L. Findell (2008), Strong sensitivity of late 21st century climate to projected changes in short-lived air pollutants, *J. Geophys. Res.*, *113*, D06102, doi:10.1029/2007JD009176.

Henze, D. K., A. Hakami, and J. H. Seinfeld (2007), Development of the adjoint of GEOS-Chem, *Atmos. Chem. Phys.*, *7*, 2413–2433.

Kawase, H., T. Nagashima, K. Sudo, and T. Nozawa (2011), Future changes in tropospheric ozone under Representative Concentration Pathways (RCPs), *Geophys. Res. Lett.*, *38*, L05801, doi:10.1029/2010GL046402.

Li, Q., D. J. Jacob, R. Park, Y. Wang, C. L. Heald, R. Hudman, R. M. Yantosca, R. V. Martin, and M. Evans (2005), North American pollution outflow and the trapping of convectively lifted pollution by upper-level anticyclone, *J. Geophys. Res.*, *110*, D10301, doi:10.1029/2004JD005039.

Moron, V., A. W. Robertson, and R. Boer (2009), Spatial coherence and seasonal predictability of monsoon onset over Indonesia, *J. Clim.*, *22*(3), 840–850, doi:10.1175/2008JCLI2435.1.

Naik, V., D. Mauzerall, L. Horowitz, M. D. Schwarzkopf, V. Ramaswamy, and M. Oppenheimer (2005), Net radiative forcing due to changes in regional emissions of tropospheric ozone precursors, *J. Geophys. Res.*, *110*, D24306, doi:10.1029/2005JD005908.

Olivier, J. G. J., J. J. M. Berdowski, J. A. H. W. Peters, J. Bakker, A. J. H. Visschedijk, and J. P. J. Bloos (2001), Applications of EDGAR including a description of EDGAR 3.2: Reference database with trend data for 1970–1995, *RIVM Rep. 773301 001*, Natl. Inst. for Public Health and the Environ., Bilthoven, Netherlands.

Parrington, M., et al. (2012), The influence of boreal biomass burning emissions on the distribution of tropospheric ozone over North America and the North Atlantic during 2010, *Atmos. Chem. Phys.*, *12*(4), 2077–2098, doi:10.5194/acp-12-2077-2012.

Sauvage, B., F. Gheusi, V. Thouret, J. P. Cammas, J. Duron, J. Escobar, C. Mari, P. Mascart, and V. Pont (2007), Medium-range mid-tropospheric transport of ozone and precursors over Africa: two numerical case studies in dry and wet seasons, *Atmos. Chem. Phys.*, *7*(20), 5357–5370, doi:10.5194/acp-7-5357-2007.

Shindell, D., and G. Faluvegi (2009), Climate response to regional radiative forcing during the twentieth century, *Nat. Geosci.*, *2*(4), 294–300, doi:10.1038/ngeo473.

Singh, K., M. Jardak, A. Sandu, K. Bowman, M. Lee, and D. Jones (2011), Construction of non-diagonal background error covariance matrices for global chemical data assimilation, *Geosci. Model Dev.*, *4*(2), 299–316, doi:10.5194/gmd-4-299-2011.

Sitch, S., P. M. Cox, W. J. Collins, and C. Huntingford (2007), Indirect radiative forcing of climate change through ozone effects on the land-carbon sink, *Nature*, *448*, 791–794, doi:10.1038/nature06059.

Stevenson, D. S., and R. G. Derwent (2009), Does the location of aircraft nitrogen oxide emissions affect their climate impact?, *Geophys. Res. Lett.*, *36*, L17810, doi:10.1029/2009GL039422.

Unger, N., T. C. Bond, J. S. Wang, D. M. Koch, S. Menon, D. T. Shindell, and S. Bauer (2010), Attribution of climate forcing to economic sectors, *Proc. Natl. Acad. Sci. U. S. A.*, *107*(8), 3382–3387, doi:10.1073/pnas.0906548107.

van der Werf, G. R., D. C. Morton, R. S. DeFries, L. Giglio, J. T. Randerson, G. J. Collatz, and P. S. Kasibhatla (2009), Estimates of fire emissions from an active deforestation region in the southern Amazon based on satellite data and biogeochemical modelling, *Biogeosciences*, *6*(2), 235–249.

van Donkelaar, A., et al. (2008), Analysis of aircraft and satellite measurements from the Intercontinental Chemical Transport Experiment (INTEX-B) to quantify long-range transport of East Asian sulfur to Canada, *Atmos. Chem. Phys.*, *8*(11), 2999–3014, doi:10.5194/acp-8-2999-2008.

Walker, T. W., et al. (2012), Impacts of midlatitude precursor emissions and local photochemistry on ozone abundances in the Arctic, *J. Geophys. Res.*, *117*, D01305, doi:10.1029/2011JD016370.

West, J. J., A. M. Fiore, L. W. Horowitz, and D. L. Mauzerall (2006), Global health benefits of mitigating ozone pollution with methane emission controls, *Proc. Natl. Acad. Sci. U. S. A.*, *103*(11), 3988–3993, doi:10.1073/pnas.0600201103.

Worden, H. M., K. W. Bowman, J. R. Worden, A. Eldering, and R. Beer (2008), Satellite measurements of the clear-sky greenhouse effect from tropospheric ozone, *Nat. Geosci.*, *1*(5), 305–308, doi:10.1038/ngeo182.

Worden, H. M., K. W. Bowman, S. S. Kulawik, and A. M. Aghedo (2011), Sensitivity of outgoing longwave radiative flux to the global vertical distribution of ozone characterized by instantaneous radiative kernels from Aura-TES, *J. Geophys. Res.*, *116*, D14115, doi:10.1029/2010JD015101.

Yevich, R., and J. A. Logan (2003), An assessment of biofuel use and burning of agricultural waste in the developing world, *Global Biogeochem. Cycles*, *17*(4), 1095, doi:10.1029/2002GB001952.

Zhang, L., D. J. Jacob, M. Kopacz, D. K. Henze, K. Singh, and D. A. Jaffe (2009), Intercontinental source attribution of ozone pollution at western US sites using an adjoint method, *Geophys. Res. Lett.*, *36*, L11810, doi:10.1029/2009GL037950.

Figure S1: Validation of the ozone DRF from single-grid cell perturbations of NOx (black), CO (red) and isoprene (green) emissions estimated using adjoint model sensitivities via comparison with the forward model estimates. Slope (m), fit line and R2 for a linear regression are indicated on the plot. Included are -50%, 10%, and 100% perturbations for emissions of NOx and 100% perturbations for emissions of CO and isoprene. Also shown (blue) are simultaneous perturbations to CO (100%) and NOx (10%) compared to the sum of the adjoint based estimates for the ozone DRF of these emissions separately.

Figure S2: The impact of (a) CO emission and (b) NMHC emission locations on ozone DRF. Areas where the radiative effectiveness ratio, reff, is greater (less) than one indicate regions where additional CO emissions would lead to an amplified (diminished) mean global ozone radiative forcing relative to the change in mean global ozone.

Figure S3: The impact of North American NOx emission locations on ozone DRF, which is the same as Fig. 3. Areas where the radiative effectiveness ratio, reff, is greater (less) than one indicate regions where additional NOx emissions would lead to an amplified (diminished) mean global ozone radiative forcing relative to the change in mean global ozone.

Figure S4: Comparison between the results from the present manuscript and those of Naik et al. [2005] for August. The panels show the following by region i: (a) global radiative forcings for a 10% perturbation to fossil fuel NOx in region i and (b) these radiative forcings normalized by the total DRF summed across all regions from panel (a). The nine regions as defined in Naik et al. [2005] are: Africa and the Mid. East (AF), Australia (AU), East Asia (EA), Former Soviet Union (FSU), India (IN), North America (NA), South America (SA), and SE Asia (SE). The relative ordering between the regions is in remarkable agreement between the two studies, indicating that even though IRK-based estimates of O3 radiative effects are on a different absolute basis than commonly considered, the relative distribution of the radiative forcing efficiencies, such as shown in Fig. 2, are likely to be more broadly applicable.

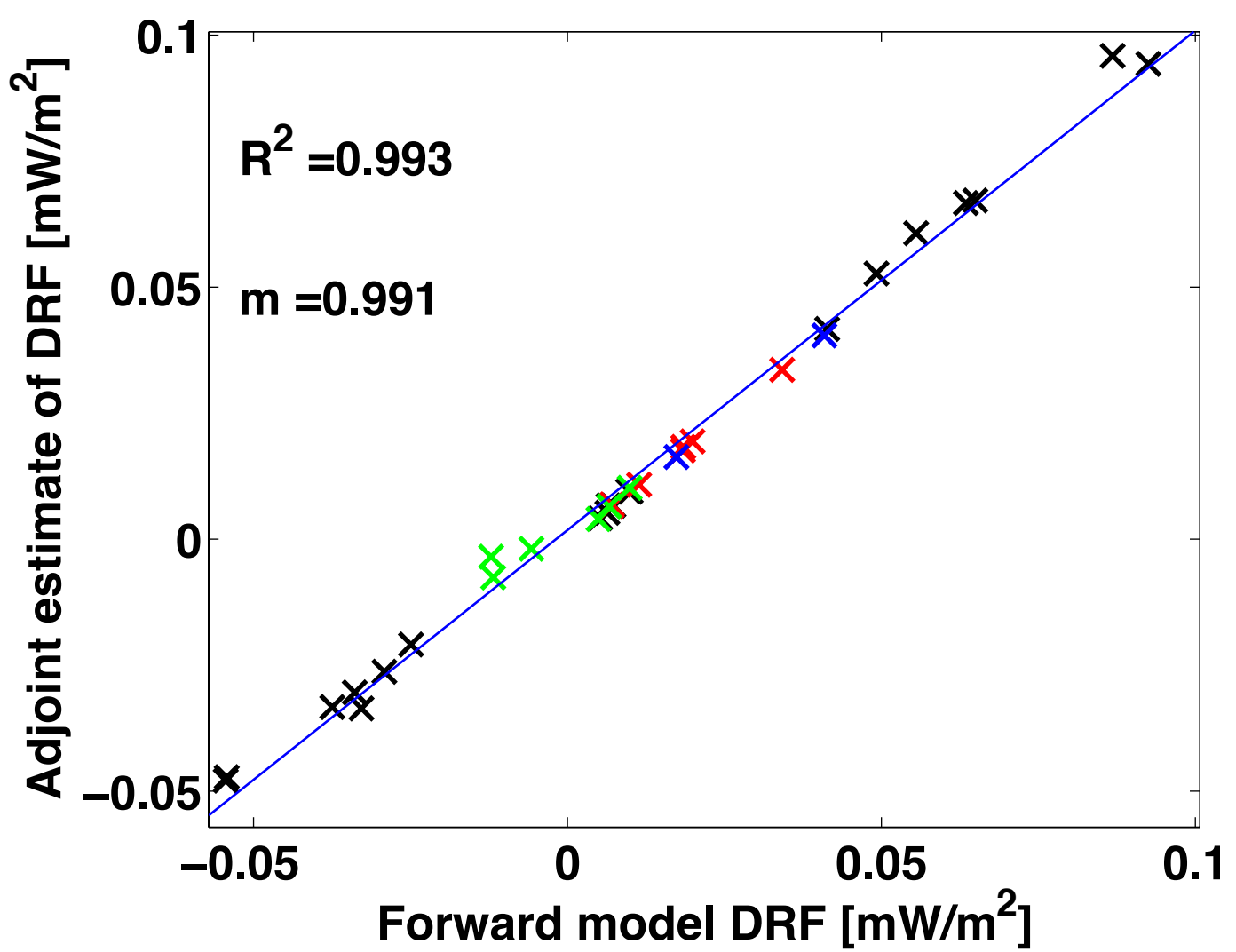
0.1
0.05
0
−0.05
−0.05
0
0.05
0.1
R^2 =0.993
m =0.991
Adjoint estimate of DRF [mW/m^2]
Forward model DRF [mW/m^2]

(a) CO

(b) NMHCs

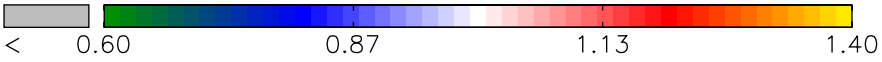

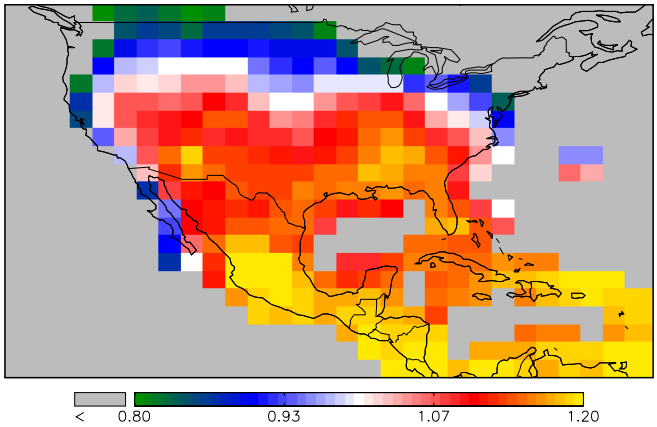
< 0.80
0.93
1.07
1.20

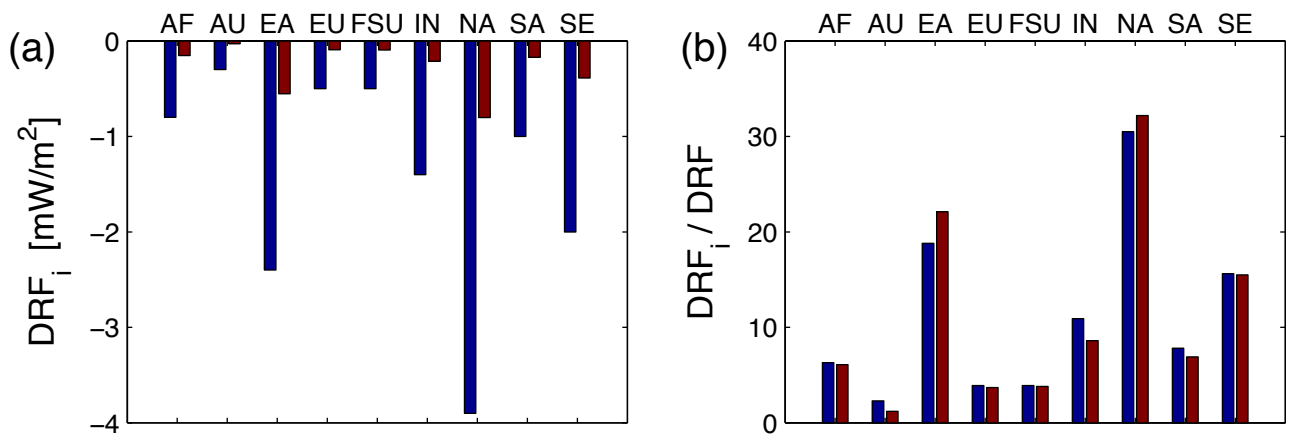
(a)
AF AU EA EU FSU IN NA SA SE
0
−1
−2
−3
−4
DRF_i [mW/m^2]
(b)
AF AU EA EU FSU IN NA SA SE
40
30
20
10
0
DRF_i / DRF

Table 1: **Supplemental** Breakdown of emissions and contributions to instantaneous tropospheric O_3 instantaneous radiative effect (IRE) for August, 2006. Percentages are listed as the amount by which each sector contributes to the total for each of the three species: NO_x, CO and NMHC.

Sector	Percent of species emitted (f_N)	Percent of IRE from species (f_{RE})
NO_x		
anthropogenic	49	24
biomass burning	16	4
biofuel	2	1
aircraft	1	3
lightning	17	59
soil	15	9
CO		
anthropogenic	42	64
biomass burning	51	31
biofuel	7	6
NMHC		
anthropogenic	69	85
biomass burning	25	11
biofuel	6	4

Table 2: **Supplemental** Location and fluxes for 27 emissions in ($Mg/km^2/yr$) centered in a $2 \times 2.5^\circ$ grid that meet the ozone DRF criterion of 0.1 ± 0.01 mW/m^2.

Lat	Lon	ENOx	ECO	ENHMC
4.0	100.0	3.27	0.86	1.02
4.0	115.0	2.02	0.67	0.71
10.0	-70.0	1.40	1.10	0.72
12.0	77.5	1.82	2.84	2.04
14.0	-90.0	0.86	0.33	0.85
14.0	102.5	1.65	1.16	1.34
20.0	85.0	1.85	1.80	1.25
22.0	85.0	2.30	2.33	1.66
24.0	85.0	2.88	2.85	2.08
24.0	87.5	3.73	3.36	2.45
24.0	117.5	4.29	2.35	1.57
26.0	-80.0	2.88	2.21	1.67
30.0	-92.5	3.06	0.66	0.78
30.0	-82.5	3.36	1.32	1.18
30.0	107.5	3.92	3.88	2.29
30.0	112.5	4.75	3.55	1.80
30.0	117.5	3.74	3.46	1.91
32.0	-95.0	2.90	0.94	0.86
32.0	112.5	5.35	3.91	1.91
34.0	-82.5	2.62	1.56	1.33
34.0	-80.0	2.65	1.41	1.16
36.0	-87.5	3.52	1.28	1.07
38.0	-77.5	4.57	2.75	1.76
40.0	-77.5	5.44	2.95	2.06
40.0	-75.0	7.31	4.17	3.78
40.0	115.0	6.85	6.18	2.65
42.0	-87.5	9.20	4.48	3.29
32.0	112.5	5.35	3.91	1.91
34.0	-82.5	2.62	1.56	1.33
34.0	-80.0	2.65	1.41	1.16
36.0	-87.5	3.52	1.28	1.07
38.0	-77.5	4.57	2.75	1.76
40.0	-77.5	5.44	2.95	2.06
40.0	-75.0	7.31	4.17	3.78
40.0	115.0	6.85	6.18	2.65
42.0	-87.5	9.20	4.49	3.29